Proceedings of the 3rd International Conference on Mathematical Physics and Computational Simulation
DOI: 10.54254/2753-8818/92/2025.21400

Designing Wind-dispersed Microfliers for Early Wildfire Warning: Aerodynamic Insights Inspired by the Glider-shaped Alsomitra Macrocarpa Seeds

Bojun Zheng[1,a,*]

[1]Tsinghua International School, Beijing, China
a. bojunzheng@gmail.com
**corresponding author*

Abstract: Wildfires not only pose a danger to humans and animals, they are also harmful to the climate and air quality by producing vast quantities of CO2. Early wildfire warning systems are crucial for minimizing environmental damage, economic losses, and threats to human life. Current unmanned aerial system for wildfire detection is limited by its low-capacity power source, which significantly reduce its flight stability and travel distance. This work designs wind-dispersed microflyer system for early wildfire warning, inspired by the glider-shaped Alsomitra Macrocarpa seeds. Famous for remarkable aerodynamic stability and exceptionally low terminal velocity, the seeds of this plant have large and papery wings and can glide long distances without reliance on gusts or updrafts. The aerodynamic analysis and wind tunnel experiment were conducted utilizing the shapes of these seeds. The analysis revealed that the Alsomitra Macrocarpa seed has an excellent aerodynamic shape with weak flow separation, which is a key reason for its superior lift-to-drag ratio. The designed microflyer with a sensor will be deployed from the air and monitor wildfire-related parameters like temperature effectively and reliably, demonstrating its potential for long-distance wind-assisted fire warning system.

Keywords: microflier, aerodynamics, Wind tunnel, CFD, wildfire

1. Introduction

Wildfires not only pose a danger to humans and animals, they are also harmful to the climate and air quality by producing vast quantities of CO2. Forest fires account for as much as 20 percent of global carbon emissions [1]. The recent forest fire in Beibei Jinyun Mountain in Chongqing city (August of 2022) involved multiple rescue forces totaling more than 20,000 people such as local firefighters, police officers and volunteers in the firefighting battles. It had a big impact on the lives of surrounding neighborhood. The last decade has witnessed a higher-than-normal frequency and magnitude of wildfires affecting thousands of people in various continents [2]. The European Space Agency estimates that approximately four million square kilometers of land are affected globally due to wildfires [3]. In the US, the National Interagency Fire Center reports 50 major wildfire events in 2022 recorded between January 1 and June 29—a number that surpasses the 10-year average—with about 192,016 acres burnt [4]. CalFire reports that the fire season in the Sierras in California has increased by 75 days each year [5]. Furthermore, *75%* of the deadliest wildfires in the state have occurred since

2000 [6]. The California Air Resources Board estimated that the state's 2020 wildfires emitted about 112 million metric tons of carbon dioxide, the highest recorded in the past decade [7]. This number is about three times higher than the second-highest emission value recorded in 2008 and is equivalent to the amount of greenhouse gases released by all the passenger vehicles in California annually. A scaled extrapolation for similar impacts on other states and countries places wildfires as one of the most urgent climate crises of this century.

Early wildfire warning systems are crucial for minimizing environmental damage, economic losses, and threats to human life. Over the years, various methods have been developed for wildfire detection, including sensor nodes, unmanned aerial vehicles (UAVs), camera networks, and satellite surveillance. Among these, UAVs stand out as flight-capable systems that can operate remotely. UAVs provide real-time, accurate data and unique vantage points that are often inaccessible, hazardous, or time-intensive for emergency responders to reach. However, a UAV system's main limitation includes low-capacity power source due to the structural constraints limiting the use of heavy energy-dense batteries. UAVs are typically equipped with a range of cameras, including video, infrared (IR), and imaging sensors, which impose limitations on their battery capacity due to the high energy demands of such equipment.

From botanic studies, wind is one of the most powerful and widely applicable means of dispersing plant seeds into air. Plants can spread their seeds through a remarkable variety of passive strategies, achieving sustained processes of natural selection. Botanists classify these methods according to their vectors for dispersal, mainly gravity, wind, water, mechanical propulsion, and animals. Inspired by wind-dispersed seeds, Kim et al. (2021) examined passive structures of aerial schemes designed for controlled, unpowered fight across natural environments or city settings [8]. Wiesemüller et al. (2022) studied bio-inspired gliders for environmental sensing [9]. The 3D shapes of seeds optimized to exploit air flow in such contexts can support stable dynamics in controlled free fall and facilitate transport over distances of hundreds of kilometers.

The seeds of Alsomitra Macrocarpa, commonly known as Javan Cucumber, which is native to the tropical forests of Maritime Southeast Asia and nearby islands, are chosen here. Remarkably, the seeds of this plant have large, papery wings and can glide long distances. Utilizing the 3D shapes of these seeds could help me to design microfliers for early wildfire warning. This work is aimed to design a novel microflyer sensor framework for fire warning that utilizes the idea of wind dispersal of plant seeds. There are very few studies on using this light and energy-saving method for early wildfire detection.

The design of seed-inspired microflyer system can be applicable to a variety of environmental sensing. The data collected by the seed-inspired microflyer system can be integrated with advanced AI weather models, such as Google's FourCastNet [10] and PunYun [11] to enhance predictive capabilities for wildfires. By providing localized and high-resolution data on critical wildfire parameters such as temperature, CO2 levels, Humidity Levels, and wind patterns, microflyer data can help refine the accuracy of these AI models, leading to better early warnings and proactive firefighting measures. With parameter changes, future applications can even optimize the microflyer's design for Mars' environmental sensing.

2. Theory analysis

2.1. Direct forces

The direct forces acting on a plate in free fall

$$\vec{F} = \overrightarrow{F_p} + \overrightarrow{F_v} + \overrightarrow{F_g} \tag{1}$$

$\vec{F}$ is the total force, $\overrightarrow{F_p}$ is the pressure force, $\overrightarrow{F_v}$ is the viscous force and $\overrightarrow{F_g}$ is the gravitational force. These forces have been described in the following subsections.

2.1.1. Pressure forces

The pressure force can be divided into two parts, which are the static flow pressure and the hydrostatic pressure.

$$\overrightarrow{F_p} = \underbrace{\int_S p d\vec{A}}_{\vec{F}_{p,S}} + \underbrace{\int_S (-\rho_f g y_{Rel}) d\vec{A}}_{\vec{F}_{p,H}} \tag{2}$$

p is the static pressure without the pressure increase due to hydrostatic effects, where the resulting surface integral is $\vec{F}_{p,S}$. The hydrostatic force is denoted $\vec{F}_{p,H}$ and $\vec{A}$ is the normal area vector, which has a direction normal to the surface and a magnitude equal to the infinitesimal surface area. This formulation allows for direct implementation in ANSYS Fluent, where $d\vec{A}$ is the area normal vector of each face on the plate, though this will take a numerical value in the simulation and the surface integral will be performed as a sum instead.

2.1.2. Viscous forces

The viscous force is integrated along the surface of the plate, where the force is equal to the dynamic viscosity multiplied with the velocity gradient at the wall inside the viscous sublayer in the direction normal to the surface, $\vec{n}$.

$$\overrightarrow{F_v} = -\int_S \left(\mu \frac{\partial \vec{u}}{\partial \vec{n}}\right) dA \tag{3}$$

2.1.3. Gravitational force

The gravitational force is

$$\overrightarrow{F_g} = m\vec{g} \tag{4}$$

$\vec{g}$ will be constant in this study of [0,-9.81] m/s^2. Furthermore, it is assumed that the plate is made of an isotropic material, so the density is assumed to be constant on the plate, thus yielding that $\overrightarrow{F_g}$ will act in the geometric center of the plate, which will coincide with the center of mass.

3. Numerical simulations

Numerical simulations of the flows past the microflyer were performed using Computational Fluid Dynamics (CFD) to study the effect of the geometry of the microflyer on its aerodynamics and flow characteristics.

3.1. Computational domain and boundary conditions

The computational domain for simulating the flow around the microflyer is shown in Fig.1. It is a rectangular box with dimensions large enough to minimize boundary effects on the flow field. The microflyer is positioned in the center to ensure symmetric flow development. A uniform inflow velocity U_∞ is applied at the inlet to simulate free-stream conditions, while the outlet is defined as a pressure outlet with zero gauge pressure. The side, bottom and top boundaries are treated as slip walls to mimic an unbounded domain. The microflyer itself is treated as a rigid no-slip wall, enabling accurate simulation of aerodynamic forces and wake dynamics. This setup ensures that the domain captures key flow features, including lift, drag, and unsteady wake behavior, without interference from boundary artifacts.

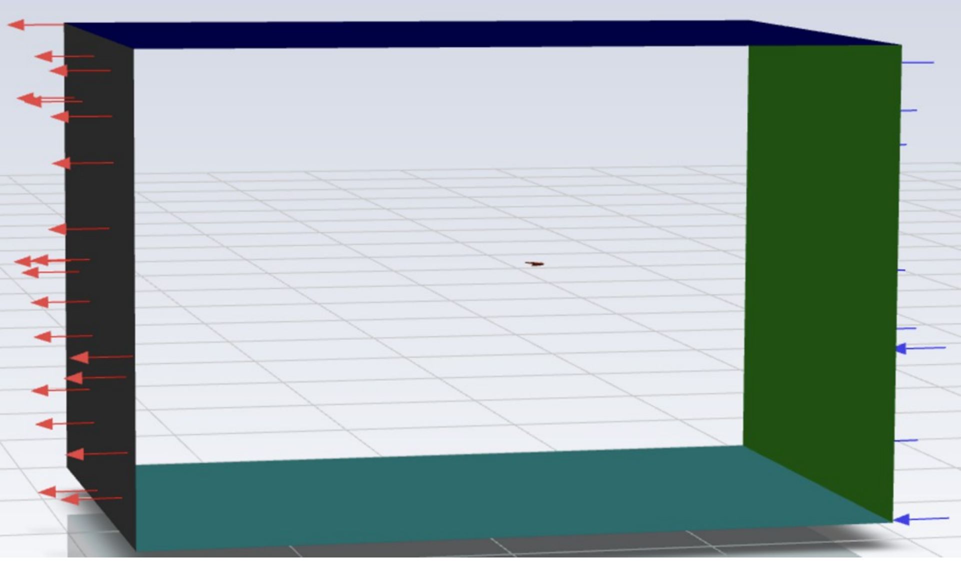

Figure 1: Computational domain.

3.2. CFD results

The coefficients of lift and drag with different wind speeds are obtained from CFD, and created a graph of Reynolds number and the coefficient of lift and drag, as shown in Fig. 2.

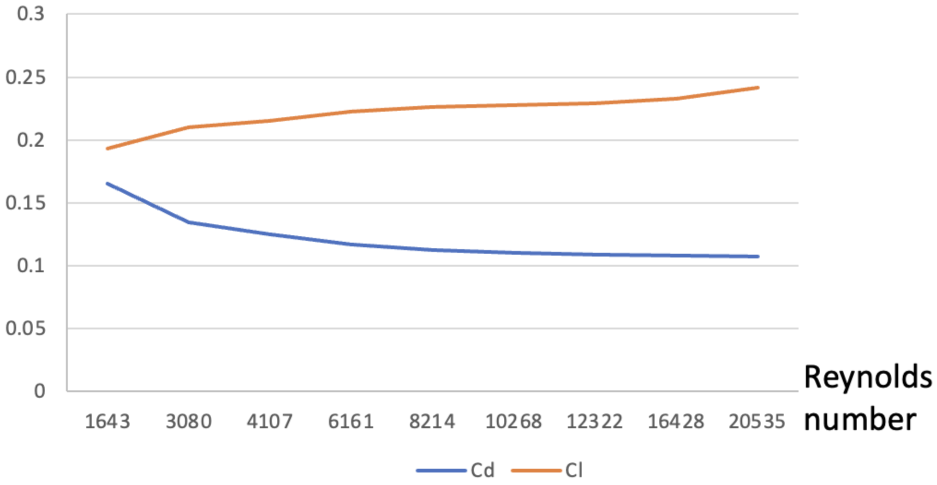

Figure 2: Drag and lift coefficients vary with Reynolds numbers.

4. Experimental test

4.1. Experiment equipments

The experiment was conducted in a DC low-speed wind tunnel with dimensions of 0.5m x 0.5m x 2.4m, as shown in Fig.3. The wind tunnel has a variable wind speed range of 0 to 45m/s, and the structure of the wind tunnel and the experimental setup are shown in the figure below. As shown in Fig.4, the seed model is installed at the center of the wind tunnel, and a 532nm green laser sheet light source illuminates the flow field from top to bottom. Smoke line devices are arranged upstream in the wind tunnel. Using electric heating, glycerin applied to fine metal wires is ignited, generating smoke particles that are blown toward the model by the wind. Under the illumination of the laser sheet light source, smoke lines are formed. These smoke lines, known as streaklines, can simulate streamlines and are used to observe the changes in the flow's movement as it passes the seed model. The upstream flow velocity of the model is measured using a Pitot tube.

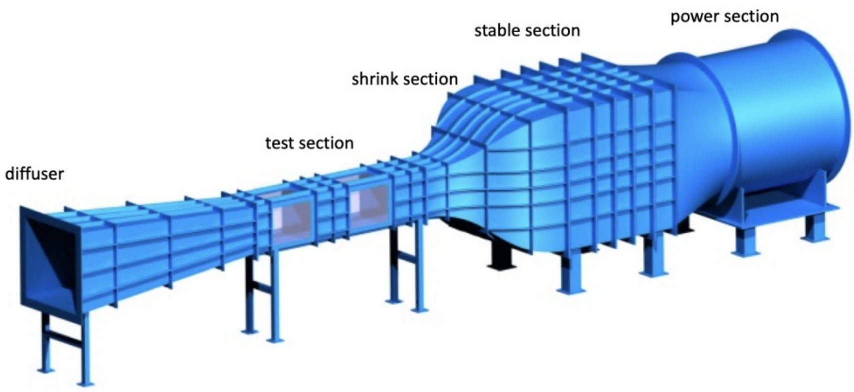

Figure 3: Schematic of the wind tunnel.

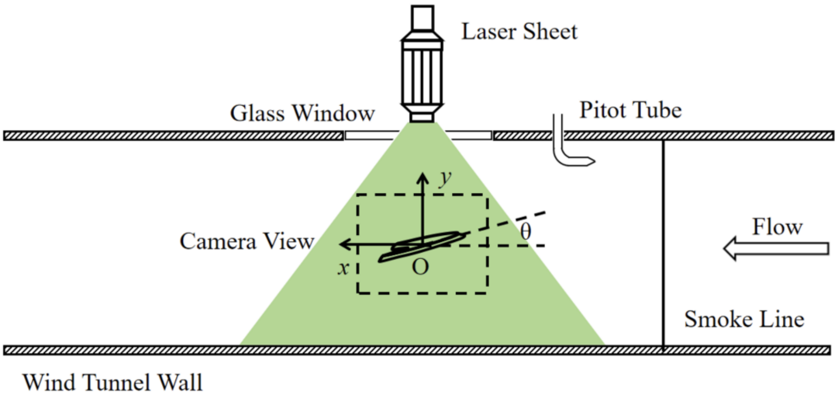

Figure 4: Illustration of Wind tunnel experiment.

4.2. Experiment details

First, based on the shape of the actual seed (Figure 5(a)), an experimental model was created using potato starch wafer paper (Figure 5(b)). The model has an average chord length of 55mm and a thickness of 0.6mm. Because laser illumination flow visualization experiments were conducted in the wind tunnel, a matte paint was applied to the surface of the model to prevent reflections. After painting, the model became slightly harder compared to before the coating, but this does not affect the flow visualization experiments.

(a) (b)

Figure 5: (a) The shape of the actual seed, and (b)experimental model created using potato starch wafer paper.

During the experiment, the incoming wind speed was set to 0.4m/s, resulting in a Reynolds number of 1500 based on the chord length. Flow images were captured using high-speed photography from the Dantec system shown in Fig. 6, with an image recording frequency of 24 frames per second and an exposure time of 500μs. Each shot lasted 1 second, allowing for the acquisition of 24 frames of 4K images.

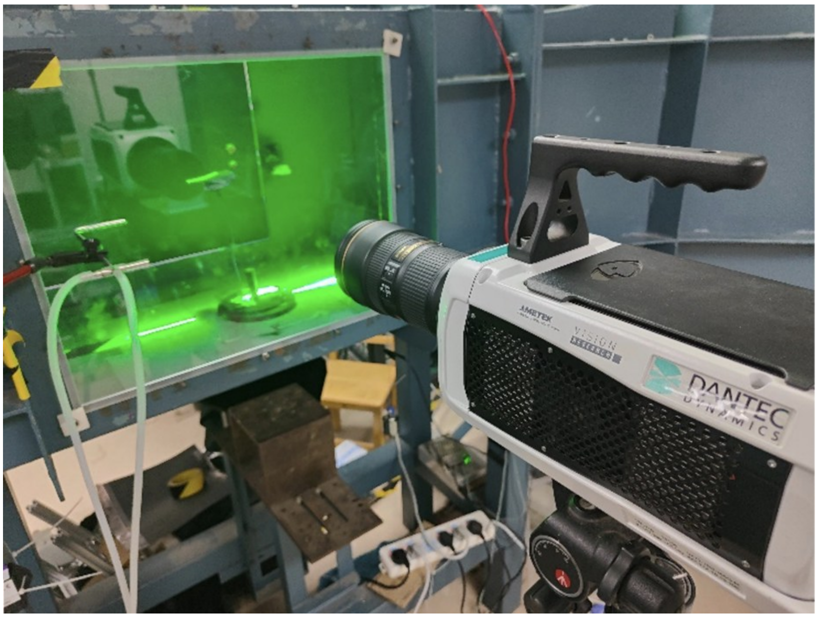

Figure 6: Flow images captured using high-speed photography from the Dantec system.

5. Results

5.1. Joukowski-Filon’s theory of aerodynamics

In 1906, Joukowski proposed his famous lift theory for two-dimensional airfoils.

$$F_L = \rho U_\infty \Gamma_\phi \tag{5}$$

Twenty years later, Filon presented a drag theory for two-dimensional airfoils.

$$F_D = \rho U_\infty Q_\Psi \tag{6}$$

In Equations (5) and (6), F is the aerodynamic force, with the subscripts L and D representing lift and drag, respectively. ρ is the air density, and U_∞ denotes the flight speed. In wind tunnel experiments, because the model is stationary, U_∞ corresponds to the incoming flow speed in the wind tunnel. Γ_ϕ represents the velocity circulation around the airfoil, while Q_Ψ represents the backflow in the vortical wake. These two equations provide the physical explanation for how lift and drag are generated—lift is proportional to the velocity circulation around the airfoil, and drag is proportional to the backflow in the vortical wake of the airfoil.

Furthermore, Prandtl provided a vortex force formula regarding the effect of vortices on objects.

$$\vec{F}_{vortex} = \rho \int_V \vec{u} \times \vec{\omega} dV\theta \tag{7}$$

In this paper, the above formulas will be used to analyze the flow visualization results.

5.2. Flow around the model effect on lift and drag

At zero angle of attack (figure 7a), the airflow passes across the entire model without any obvious flow separation, and only some distance downstream of the trailing edge does the flow curl and form a shedding vortex, indicating very low drag. Because a vortex forms near the trailing edge, the velocity circulation theorem indicates that there is a non-zero circulation around the model. According to Joukowski's lift theory, the paper model therefore generates a non-zero lift.

When the angle of attack is -10 degrees (figure 7b), the flow along the lower surface first separates, then reattaches to the bottom of the model, and finally separates at the trailing edge. Overall, the flow separation is weak, suggesting that the drag is lower than at zero angle of attack. Once the model goes into a diving flight, its speed can become noticeably higher than it is at zero angle of attack.

When the angle of attack is 10 degrees (figure 7c), the flow separates at different locations on the upper and lower surfaces. Near the upper surface, the flow separates at the leading edge, creating relatively large-scale vortices. On the lower surface, the flow only separates at the trailing edge, producing vortices that rotate opposite to those generated at the leading edge. These two vortices meet near the trailing edge and then leave the model, exerting dynamic forces that can cause instability in the model's orientation. However, at this angle, the large-area flow separation on the upper surface increases lift. At the same time, a large-scale vortex forms on the back side of the model, causing backflow, which in turn increases drag compared to the zero angle of attack condition.

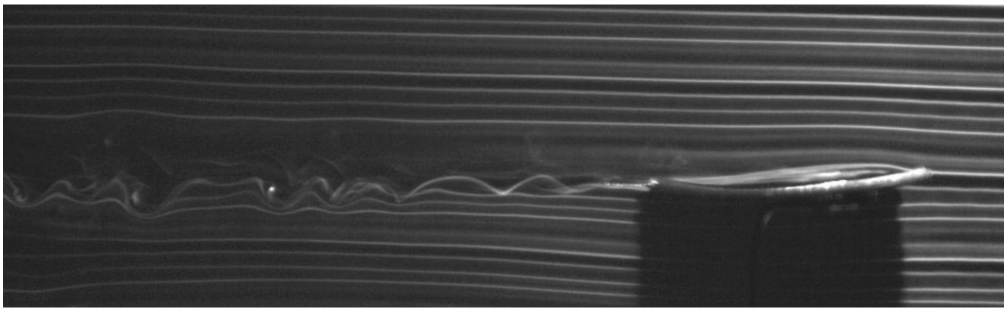

(a)

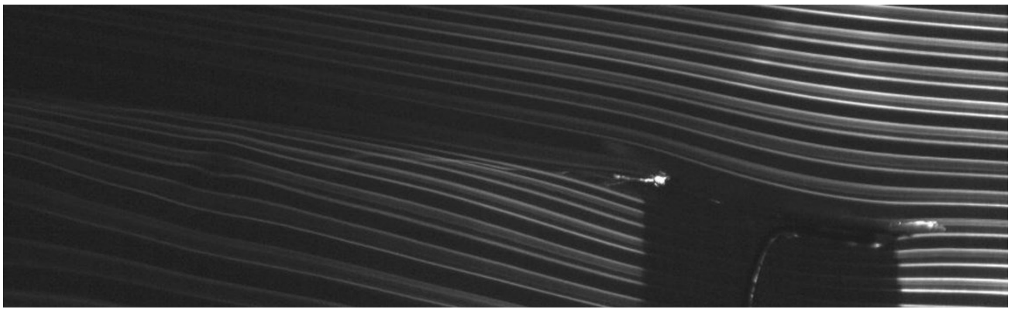

(b)

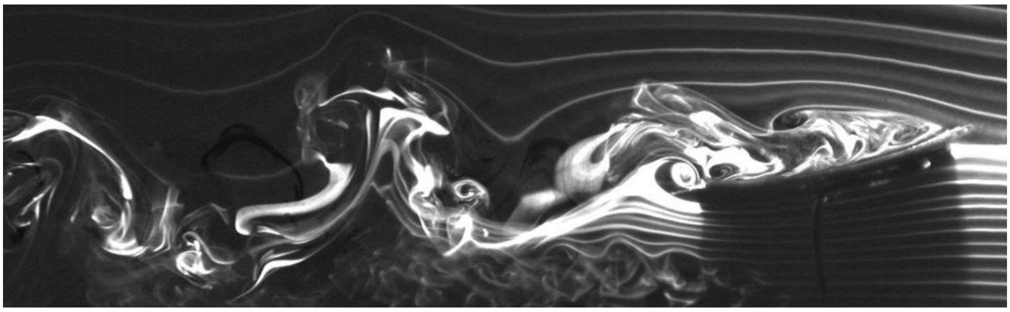

(c)

Figure 7: Flow visualizations using the smoke lines at different angles of attack: (a) zero degree, (b) -10 degrees, and (c) 10 degrees.

5.3. Analysis of Alsomitra Macrocarpa Seed Flight Stability

In reality, the seeds of Alsomitra macrocarpa resemble thin, flexible wing-like structures. During flight, when encountering changes in angle of attack or airflow fluctuations, they undergo deformation and slight vibrations. These deformations and vibrations counteract the aerodynamic moments and prevent the seeds from rolling over mid-flight. This is the primary reason why Alsomitra macrocarpa seeds maintain stable flight.

5.4. Discussion

In this experiment, only the flow around the central portion of the model was investigated. Because the leading and trailing edges of the model have a curved-blade shape, the actual flow will have different separation locations along the trailing edge. The separated vortices may form curved vortex tubes whose axes resemble the shape of the trailing edge boundary. Using Prandtl’s vortex force formula, as the vortex tubes move downstream, they can induce lift.

Although the experimental model differs from the actual Alsomitra macrocarpa seed in some ways, it preserves the seed’s leading and trailing edge shapes, as well as its softness and thinness. Consequently, the flow characteristics around this model basically reflect those of the real seed. Thus, the analysis and conclusions drawn from this experiment provide valuable insights into how the seed maintains stable flight and is able to glide over long distances.

6. Conclusion

By imitating the shape of Alsomitra Macrocarpa seeds, a wind tunnel experiment model was designed. Flow visualization techniques were used to observe how the airflow moves and changes as it passes over the model, and the effects of the airflow on the model’s aerodynamic forces were analyzed. The analysis shows that Alsomitra Macrocarpa seeds have an excellent aerodynamic profile, with relatively weak flow separation—an important reason for their high lift-to-drag ratio. During flight, the elastic vibrations and deformations of the seed's flexible wing structure counteract aerodynamic moments and suppress potential rolling motions. In summary, by simulating the shape of Alsomitra Macrocarpa seeds, it is possible to design a glider that can achieve stable, unpowered flight over long distances.

References

[1] BOSCH, Preventing wildfires with a small sensor, https://www.bosch.com/stories/early-forest-fire-detection-sensors/

[2] Mohapatra, A. and Trinh, T., Early wildfire detection technologies in practice—A review Sustainability 2022, 14, 12270.

[3] The European Space Agency. New Long-Term Dataset to Analyse Global Fire Trends; The European Space Agency: Paris, France, 2021.

[4] National Fire News: National Preparedness Level 2; National Interagency Fire Center: Boise, ID, USA, 2022.

[5] Mohapatra, A. and Trinh, T., Early wildfire detection technologies in practice—A review Sustainability 2022, 14, 12270.

[6] California Department of Fish and Wildlife. 2022. Available online: https://wildlife.ca.gov/Science-Institute/Wildfire-Impacts

[7] California Air Resources Board. 2020. Available online: https://ww2.arb.ca.gov/ghg-inventory-data (accessed on 01 December 2024)

[8] Kim, B.H., et al. Three-dimensional electronic microfliers inspired by wind-dispersed seeds. Nature Vol 597, 503-523, 2021.

[9] Wiesemüller F, Meng Z, Hu Y, Farinha A, Govdeli Y, Nguyen PH, Nyström G and Kovač M, 2022, Transient bio-inspired gliders with embodied humidity responsive actuators for environmental sensing. Front. Robot. AI 9:1011793. doi: 10.3389/frobt.2022.1011793

[10] Pathak, J., et al. FourCastNet: A Global data-driven high-resolution weather model using adaptive fourier neural operators. (2022) https://doi.org/10.48550/arXiv.2202.11214

[11] Zhu, S., et al. PuYun: Medium-range global weather forecasting using large kernel attention convolutional networks. (2024) https://doi.org/10.48550/arXiv.2409.02123